Pollitz, F. F., Cattania, C. (2017): Connecting crustal seismicity and earthquake-driven stress evolution in Southern California. - *Journal of Geophysical Research*, *122*, 8, pp. 6473—6490.

DOI: http://doi.org/10.1002/2017JB014200

AGU PUBLICATIONS

JGR

Journal of Geophysical Research: Solid Earth

RESEARCH ARTICLE
10.1002/2017JB014200

Key Points:
- A catalog spanning three decades of Southern California seismicity is consistent with the Coulomb rate-state stressing model
- Spatial patterns of seismicity evolved systematically following the 1992 Landers, California, earthquake
- Both static and viscoelastic stress transfer mechanisms are effective at triggering seismicity

Correspondence to:
F. F. Pollitz,
fpollitz@usgs.gov

Citation:
Pollitz, F. F., and C. Cattania (2017), Connecting crustal seismicity and earthquake-driven stress evolution in Southern California, *J. Geophys. Res. Solid Earth*, *122*, 6473–6490, doi:10.1002/2017JB014200.

Received 12 MAR 2017
Accepted 18 JUL 2017
Accepted article online 23 JUL 2017
Published online 14 AUG 2017

Connecting crustal seismicity and earthquake-driven stress evolution in Southern California

Fred F. Pollitz[1] **and Camilla Cattania**[2]

[1]USGS, Menlo Park, California, USA, [2]GeoForschungsZentrum, Potsdam, Germany

Abstract Tectonic stress in the crust evolves during a seismic cycle, with slow stress accumulation over interseismic periods, episodic stress steps at the time of earthquakes, and transient stress readjustment during a postseismic period that may last months to years. Static stress transfer to surrounding faults has been well documented to alter regional seismicity rates over both short and long time scales. While static stress transfer is instantaneous and long lived, postseismic stress transfer driven by viscoelastic relaxation of the ductile lower crust and mantle leads to additional, slowly varying stress perturbations. Both processes may be tested by comparing a decade-long record of regional seismicity to predicted time-dependent seismicity rates based on a stress evolution model that includes viscoelastic stress transfer. Here we explore crustal stress evolution arising from the seismic cycle in Southern California from 1981 to 2014 using five $M \geq 6.5$ source quakes: the *M*7.3 1992 Landers, M6.5 1992 Big Bear, *M*6.7 1994 Big Bear, *M*7.1 1999 Hector Mine, and *M*7.2 2010 El Mayor-Cucapah earthquakes. We relate the stress readjustment in the surrounding crust generated by each quake to regional seismicity using rate-and-state friction theory. Using a log likelihood approach, we quantify the potential to trigger seismicity of both static and viscoelastic stress transfer, finding that both processes have systematically shaped the spatial pattern of Southern California seismicity since 1992.

1. Introduction

Crustal seismicity is thought to be linked to earthquake-driven transient stress changes through numerous mechanisms, including dynamic stresses (during or shortly after seismic wave propagation), static stress changes (instantaneous and long lived), and postseismic stress changes, which are slowly evolving and may arise from a combination of afterslip and viscoelastic relaxation of the lower crust and mantle [*Freed*, 2005]. The importance of both dynamic stressing and static stress transfer for earthquake triggering is well documented [e.g., *Harris*, 1998; *Stein*, 1999; *Steacy et al.*, 2005], while viscoelastic stress transfer has been suggested as an important mechanism in a few case studies [e.g., *Freed and Lin*, 2001; *Zeng*, 2001; *Pollitz and Sacks*, 2002; *DeVries et al.*, 2016].

Toda et al. [2005] construct a model of time-dependent seismicity rate in Southern California that accounts for coseismic stress steps following selected $M \geq 5.5$ source events, and they relate them to seismicity rate via a rate-and-state friction model. They find a substantial correlation between predicted and observed seismicity rate in a set of cells spanning the region, with time-dependent correlation coefficients ~0.5. These correlations are generally highest for about 1 year following the largest ($M > 7$) source quakes, but they are consistently elevated, relative to correlations obtained with background seismicity, for the entire 17 year study period, suggesting that static stress changes have a systematic effect on seismicity that persists for decades.

Here we construct models of crustal stress evolution in Southern California in order to test the viability of static and viscoelastic stress transfer from several $M \gtrsim 7$ source earthquakes over a period of decades and compute the spatiotemporal distribution of triggered seismicity with a rate-and-state friction approach [*Dieterich*, 1994]. Using a catalog of Southern California seismicity from 1981 to 2014 (E. Hauksson catalog available online), edited to 2288 $M \geq 3.5$ events (Figure 1), we apply the rate-and-state friction-based log likelihood (LL) function [e.g., *Zhuang et al.*, 2012; *Cattania et al.*, 2015] to evaluate the ability of stress evolution models to explain the observed seismicity. One candidate model accounts for static stress steps at the times of the four $M \geq 6.7$ events: the *M*7.3 1992 Landers, *M*6.7 1994 Northridge, *M*7.1 1999 Hector Mine, and *M*7.2 El Mayor-Cucapah earthquakes, and the *M*6.5 1992 Big Bear earthquake which was part of the Landers sequence (Figure 1). A second model accounts for the static stress steps plus viscoelastic stress transfer. The patterns of

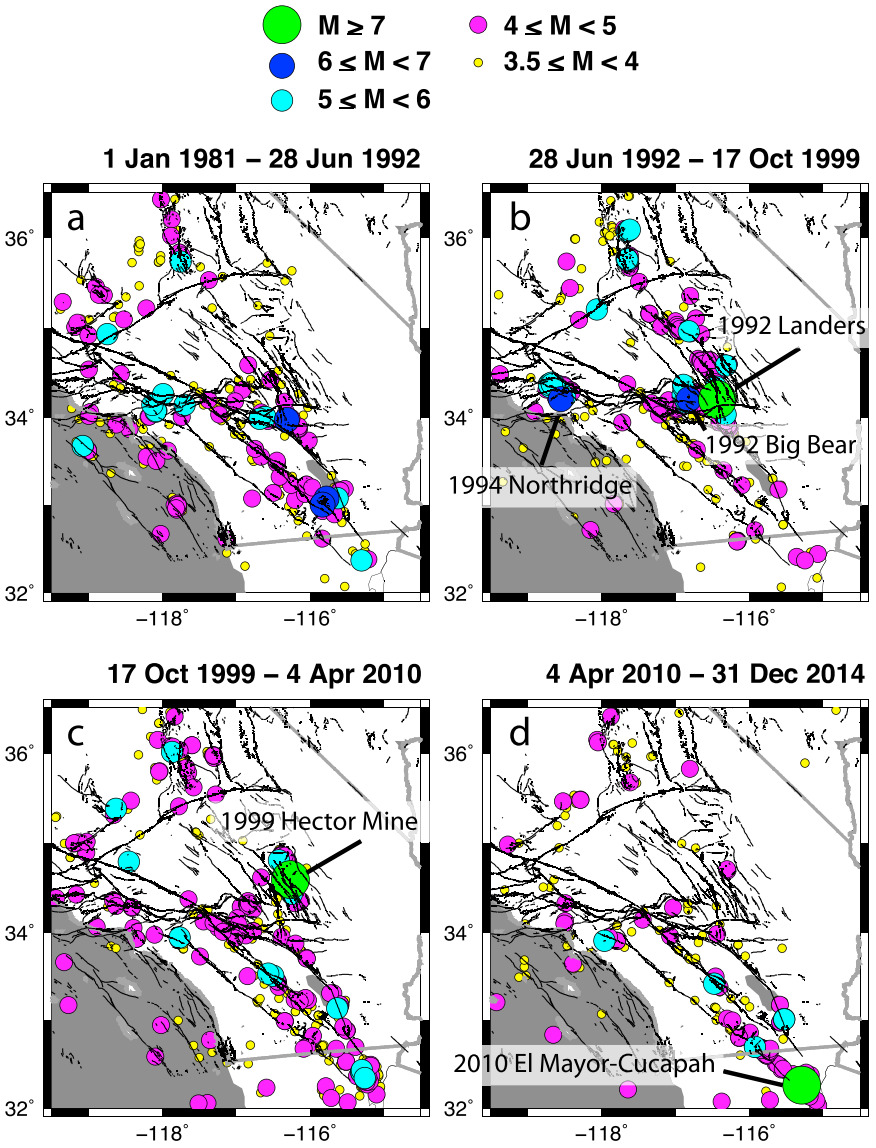

Figure 1. $M \geq 3.5$ seismicity in Southern California in selected time periods: (a) 1981 to just before the 1992 Landers quake, (b) just after the 1992 Landers quake to just before the 1999 Hector Mine quake, (c) just after the 1999 Hector Mine quake to just before the 2010 El Mayor-Cucapah quake, and (d) just after the 2010 El Mayor-Cucapah quake to 2014. Faults from the U.S. Geological Survey (USGS) Quaternary faults database are superimposed.

LL from these two models and a null model provide guidance on the physical mechanisms controlling regional seismicity. In particular, we shall test whether the difference in LL among these three models (information gain) is significant, providing guidance on whether static and/or viscoelastic stress transfer has a tangible effect on regional seismicity for decades following a sequence of large main shocks.

2. Coulomb Rate-and-State Model of Time-Dependent Seismicity Rate

The Coulomb failure function is defined as follows:

$$\mathrm{CFF} = \tau - \mu\sigma_{\mathrm{eff}}, \tag{1}$$

where τ is shear stress on the fault, μ is the coefficient of friction, and $\sigma_{\mathrm{eff}} = \sigma - p$ is the effective normal stress, where σ is the normal stress and p is the pressure. Coulomb failure function (CFF) tracks the evolving transient loading of a fault with time, and under the Coulomb failure hypothesis positive CFF is expected to lead to increased seismicity rates and negative CFF to reduced seismicity rates.

Rate-and-state friction theory provides a relation between the evolving tectonic stress field and seismicity rates. An increase in stress will lead to a temporary increase in seismicity rate at a time scale that is controlled by constitutive properties of the faults and conversely for a stress decrease. This is quantified using a modified version of equation (B14) of *Dieterich* [1994] for the evolution of the state variable γ:

$$\mathrm{d}\gamma = \frac{1}{A\sigma}\left[\mathrm{d}t - \gamma \mathrm{d}S\right], \tag{2}$$

where A is a fault constitutive parameter and $S = \tau - (\mu - \alpha)\sigma_{\mathrm{eff}}$, where α is a positive dimensionless parameter [*Linker and Dieterich*, 1992]. Changes in S can be interpreted as changes in CFF [*Hainzl et al.*, 2010; *Cattania et al.*, 2015, and references therein] by assuming that pore pressure changes are related to normal stress changes via a proportionality constant (Skempton's coefficient B), $\mathrm{d}p = B\mathrm{d}\sigma$ and defining an effective coefficient of friction $\mu' = (\mu - \alpha)(1 - B)$ so that $\mathrm{d}S = \mathrm{d}\tau - \mu'\mathrm{d}\sigma$.

Define $\dot{\tau}_r$ be the background stressing rate and t_a to be a time constant given by

$$t_a = \frac{A\sigma}{\dot{\tau}_r}. \tag{3}$$

We define $\delta S(t)$ to be the perturbation in Coulomb stress arising from time-dependent variations in the tectonic stress field, e.g., coseismic stress steps and postseismic stress evolution contributed by afterslip or viscoelastic relaxation of the lower crust and mantle. After a time step Δt, the stress perturbation increases an amount

$$\Delta S = \delta S(t + \Delta t) - \delta S(t) \tag{4}$$

and stressing rate is

$$\dot{S} = \dot{\tau}_r + \frac{\Delta S}{\Delta t}. \tag{5}$$

From equation (2), assuming constant $\dot{S}$ over the time interval $(t, t + \Delta t)$, the state variable evolves from time t to $t + \Delta t$ according to

$$\gamma(t + \Delta t) = \left(\gamma(t) - \frac{1}{\dot{S}}\right)\exp\left(-\frac{\dot{S}}{\dot{\tau}_r}\frac{1}{t_a}\Delta t\right) + \frac{1}{\dot{S}}. \tag{6}$$

This is equivalent to equation (5) of *Toda et al.* [2005], with the provision that they include no postseismic stressing (i.e., $\Delta S/\Delta t = 0$ between source quakes) and thus replace $1/\dot{S}$ with $1/\dot{\tau}_r$ in equation (6).

The time-dependent seismicity rate R is given by [*Dieterich*, 1994, equation (11)]

$$R = \frac{r}{\gamma\dot{\tau}_r}, \tag{7}$$

where r is the background seismicity rate, here estimated from catalog seismicity via equation (8). For a stress step occurring over a very short time interval (i.e., the limit as Δt approaches zero) and followed by possibly different stressing rate $\dot{S}$ that is assumed constant, equations (4) to (7) are equivalent to equation (12) of *Dieterich* [1994]. Hence, they share the property of that solution that at sufficient time after a stress step and under a constant stressing rate, γ tends to the steady state value $1/\dot{S}$ and the seismicity rate R tends to the value $r \times (\dot{S}/\dot{\tau}_r)$. However, equations (4)–(7) provide a general prescription for relating seismicity rate to evolving stress given a time series of stressing rate that may include both episodic stress steps as well as more slowly evolving postseismic and interseismic stress.

3. Three Decades of Seismicity

We utilize a catalog of seismicity in Southern California over the period 1981 to 2014 presented online by E. Hauksson (http://scedc.caltech.edu/research-tools/alt-2011-yang-hauksson-shearer.html). It is an update of the HTS_catalog_2011 presented by *Yang et al.* [2012]. The Hauksson catalog has refined locations based on absolute and differential body wave picks. The data set includes 186,993 events down to magnitude 1.0, and

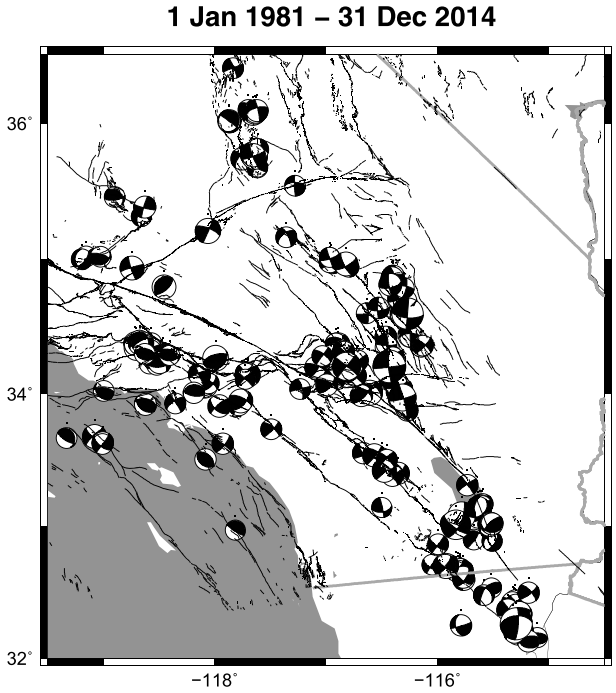

Figure 2. Focal mechanisms of $M \geq 4.5$ quakes from 1981 to 2014 taken from the E. Hauksson online catalog.

examination of its cumulative magnitude distribution indicates that it is complete down to about magnitude 2.0. We conservatively choose a minimum magnitude of 3.5, which reduces the number of catalog events to 2288. The epicenters of these events in various time periods are shown in Figure 1 and focal mechanisms of $M \geq 4.5$ events in Figure 2. The seismicity is concentrated around the San Andreas fault (SAF) and adjacent San Jacinto and Elsinore faults, the Eastern California Shear Zone, and southwest of the San Andreas fault near the Big Bend. Three $M \geq 7$ events occur during this time period (Figures 1b–1d), and each is followed by a great number of $M \geq 3.5$ aftershocks. The overall seismicity pattern is characterized by strong activity within the Eastern California Shear Zone (ECSZ), i.e., the 1992 and 1999 rupture zones and their northward extension across the Garlock fault to the Owens Valley fault, the southern SAF, especially south of 34°N, the San Jacinto fault, and the region west of the SAF near the Big Bend.

We determine background seismicity rate r at points $\mathbf{r}$ in the study area via the following Gaussian smoothing scheme introduced by *Helmstetter et al.* [2007]:

$$r(\mathbf{r}) = \frac{1}{T}\frac{1}{2\pi D^2(\mathbf{r})}\sum_i \exp\left(-\frac{1}{2}\left[|\mathbf{r}-\mathbf{r}_i|/D(\mathbf{r})\right]^2\right), \tag{8}$$

where the i summation is over all catalog events in the $T = 11.5$ year long interval before the Landers earthquake, $|\mathbf{r} - \mathbf{r}_i|$ is the horizontal distance between target point $\mathbf{r}$ and catalog hypocenter #i, $D(\mathbf{r})$ is a Gaussian smoothing distance, and $2\pi D^2(\mathbf{r})$ is a normalizing constant. D is initially set to 20 km, but if the minimum $|\mathbf{r} - \mathbf{r}_i|$ is greater than 20 km, then following *Helmstetter et al.* [2007], D is set equal to the distance to the second closest catalog hypocenter. The events retained in the summation of equation (8) are first restricted to the pre-Landers period, i.e., from 1981 to 28 June 1992. They are further edited with the declustering scheme presented by *Knopoff* [2000], which is similar to the original *Gardner and Knopoff* [1974] declustering scheme. *Cattania* [2015] notes that declustering space and time windows have the effect of suppressing background events that would have occurred during these windows. Hence, retained events that fall within one or more aftershock spatial windows—but outside the associated temporal windows—are assigned a weight equal to $T_{\text{tot}}/(T_{\text{tot}} - T_{\text{ds}})$, where T_{ds} is the total time spanned by aftershock windows. We use equation (8) to estimate background seismicity rates at the 2288 $M \geq 3.5$ catalog epicenters and at 3000 randomly distributed points in a region encompassing most of the seismically active part of Southern California (Figure 3). Specifically, the random hypocenters occupy a conical volume centered on 34.0°N, 117.3°W of radius 2.75 geocentric degrees between Earth's surface and 20 km depth. The resulting pattern of r is concentrated along the southern SAF and ECSZ. We also assess the uncertainty in r by determining it in five consecutive time intervals of equal length spanning the period 1981 to 28 June 1992 then evaluating its variance. The resulting standard deviation shown in Figure 3c is generally about a factor of 2 to 5 smaller than r itself. Note that such uncertainty in r is of no consequence when evaluating the metrics that we shall use to quantitatively test our stress evolution model, i.e., seismicity rate gain R/r in section 4.3 or information gain in section 5.

4. Application to Southern California Seismicity

4.1. Time-Dependent Stress

The parameters used to quantify seismicity rates, stress, and statistical quantities derived therefrom in this and the preceding sections are summarized in Table 1. For simplicity, in each trial simulation we assume that both $A\sigma$ and t_a (equation (3)) are spatially uniform and do not change with time.

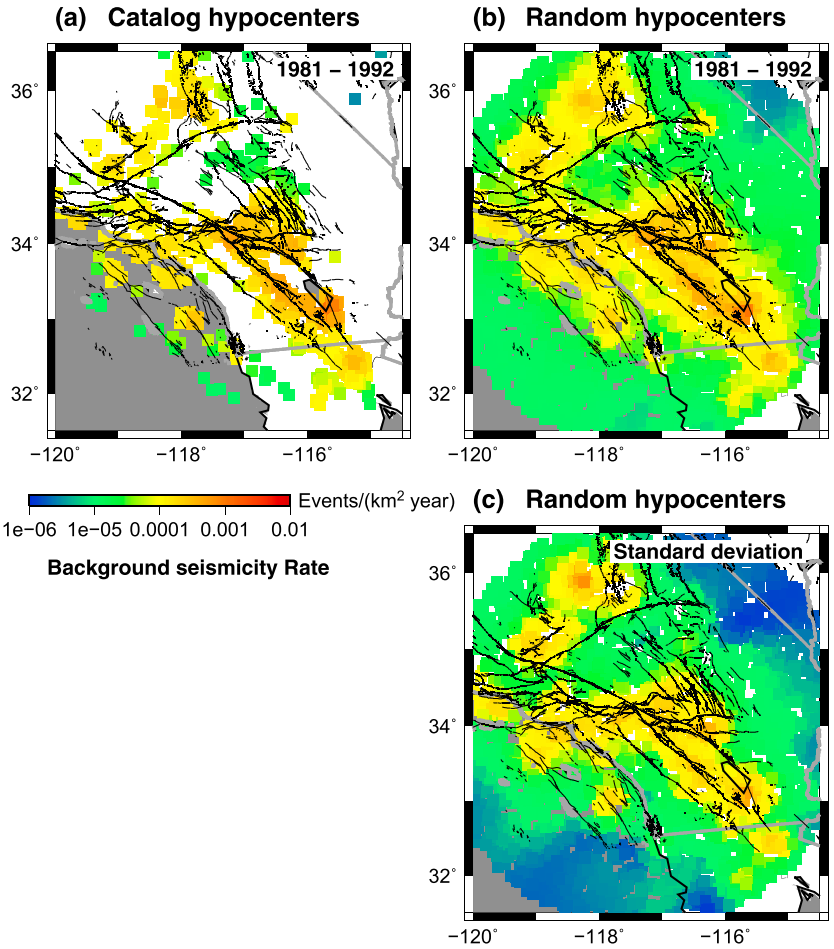

Figure 3. Background seismicity rate in Southern California at (a) 2288 $M \geq 3.5$ catalog epicenters and (b) 3000 randomly distributed points, using the E. Hauksson online catalog edited to $M \geq 3.5$ events during the 11.5 years prior to the Landers quake (i.e., 1 January 1981 to 28 June 1992). (c) The standard deviation of the seismicity rate shown in Figure 3b based on finer sampling of the background period. In Figure 3b the random points are distributed within an area of radius 2.75 geocentric degrees centered on 34.0°N, −117.3°E over the depth range 0–20 km. Here and in subsequent figures, each epicenter or point is plotted with a square for visibility. Outlines of source faults are shown with thick black lines in each subplot.

Time-dependent stress perturbation δS is generated by major source earthquakes. We utilize the five $M \geq 6.5$ sources to have occurred in Southern California over the past three decades: *M*7.3 1992 Landers, *M*6.5 1992 Big Bear, *M*6.7 1994 Northridge, *M*7.1 1999 Hector Mine, and *M*7.2 El Mayor-Cucapah earthquakes (Figure 1). Simplified rupture models are employed for these sources: a seven-plane approximation to the

Table 1. Summary of Model Parameters and Results

Parameter	Name	Values	Equations	Figures
r	Background seismicity rate	variable	(8)	3
$\dot{\tau}_r$	Background stressing rate	variable	—	6
γ	State parameter	variable	(2), (6), and (11)	—
R	Time-dependent seismicity rate	variable	(7) and (12)	8–13
t_a	Aftershock decay time	5000 days	(3)	8–13
		variable	(3)	14–16
μ'	Effective coefficient of friction	0.2	(9)	8–16
		0.6	(9)	11 and 13
LL	Log likelihood	—	(10)	—
I	Information gain	—	(13)	14–16

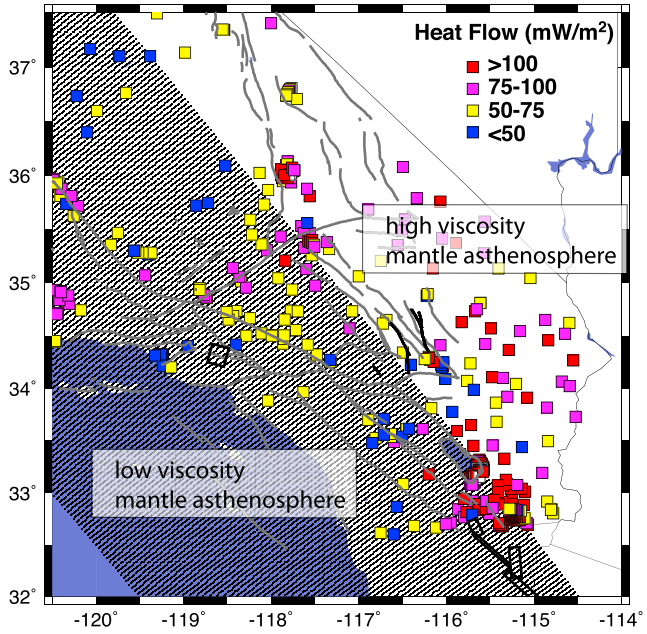

Figure 4. Two-dimensional structure of *Pollitz* [2015], characterized by the relatively high viscosity northeast domain (unshaded) and relatively low viscosity southwest domain (shaded) (Figure 5). Thick black line segments denote the source earthquakes considered in this study. Superimposed is heat flow in Southern California from the USGS online database. The lack of correlation of high heat flow with low-viscosity mantle over most of the area was interpreted by *Pollitz* [2015] to arise from lateral variations in mantle hydration.

Wald and Heaton [1994] rupture model for the Landers quake, a 24-plane approximation to the *Jónsson et al.* [2002] rupture model for the Hector Mine quake [*Pollitz*, 2015], and a four-plane approximation to the *Wei et al.* [2011] rupture model for the El Mayor-Cucapah quake. We append the *M*6.5 1992 Big Bear earthquake, a large early aftershock of the Landers earthquake, and the *M*6.7 1994 Northridge earthquake, using one-fault plane models provided by *Jones et al.* [1993] and *Hauksson et al.* [1995], respectively.

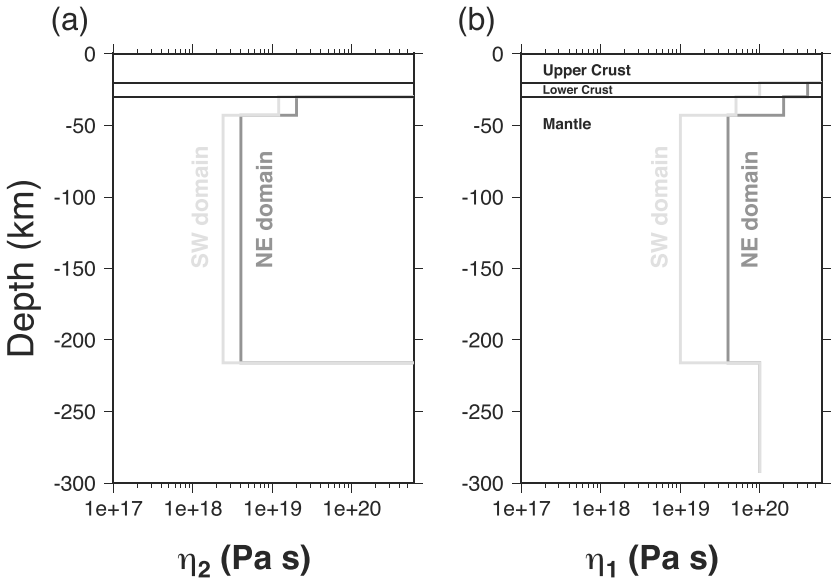

Figure 5. Optimal 2-D Burgers body model determined in a grid search. (a and b) Depth-dependent transient and steady state viscosity η_2 and η_1, respectively, for the preferred northeast and southwest structures presented in *Pollitz* [2015]. Both the northeast and southwest domains have the same elastic structure and the same transient shear modulus $\mu_2 = 70$ GPa in the mantle. The lower crust is assumed to be a Maxwell solid.

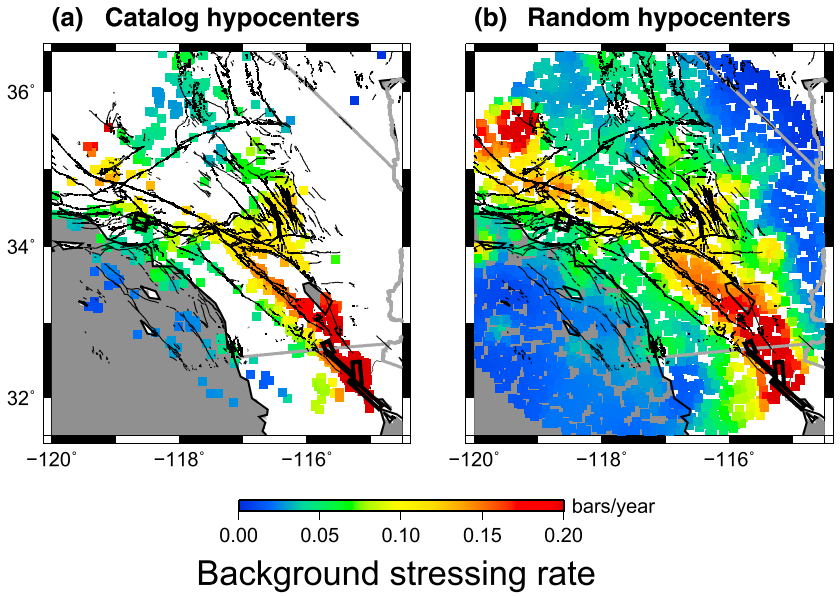

Figure 6. Background stressing rate $\dot{\tau}_r$ at (a) catalog hypocenters and (b) random hypocenters derived from the GPS velocity field [*Pollitz et al.*, 2010]. Outlines of source faults are shown with thick black lines in each subplot.

Stress evolution beginning at the time of the Landers quake is calculated on the preferred 2-D viscoelastic structure presented by *Pollitz* [2015]. This structure consists of two welded 1-D viscoelastic structures, a relatively high viscosity "northeast domain" and low-viscosity "southwest domain" (Figures 4 and 5). Static and postseismic deformation generated by the $M \geq 6.5$ sources quakes on this structure are calculated using a 2.5-D spectral element code [*Pollitz*, 2014]. This yields time series of the stress tensor perturbation $\boldsymbol{\sigma}(\mathbf{r}, t)$ throughout the study volume, again defined as an area 2.75 geocentric degrees in radius centered on 34.0°N, −117.3°E and spanning the depth range 0–20 km.

The time series of stress tensor perturbations $\boldsymbol{\sigma}$ are used to determine time series of perturbation in Coulomb stress at a given location via [*King et al.*, 1994]

$$S = \hat{\boldsymbol{n}} \cdot \boldsymbol{\sigma} \cdot \hat{\boldsymbol{s}} + \mu' \left(\hat{\boldsymbol{n}} \cdot \boldsymbol{\sigma} \cdot \hat{\boldsymbol{n}} \right), \tag{9}$$

where $\hat{\boldsymbol{n}}$ represents the normal unit vector to a receiver fault and $\hat{\boldsymbol{s}}$ the corresponding slip vector and μ' is the effective coefficient of friction.

4.2. Log Likelihood Function

We fit rate-and-state parameters to the observed seismicity by maximizing a log likelihood (LL) function, which is defined as the probability of an observed set of quakes occurring given the overall rate of earthquake production predicted by the model within a specified volume. As quantified by *Ogata* [1983], it is given by

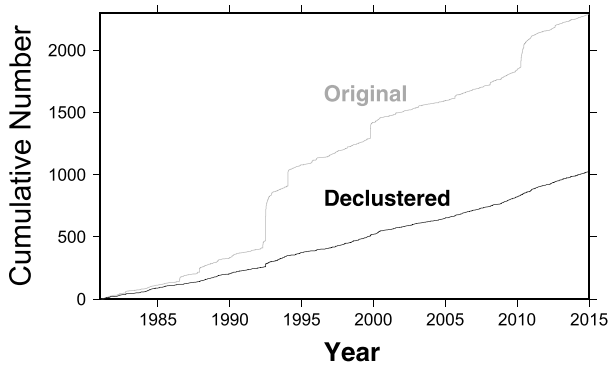

Figure 7. Cumulative $M \geq 3.5$ seismicity using the original catalog (gray curve) and declustered catalog (black curve).

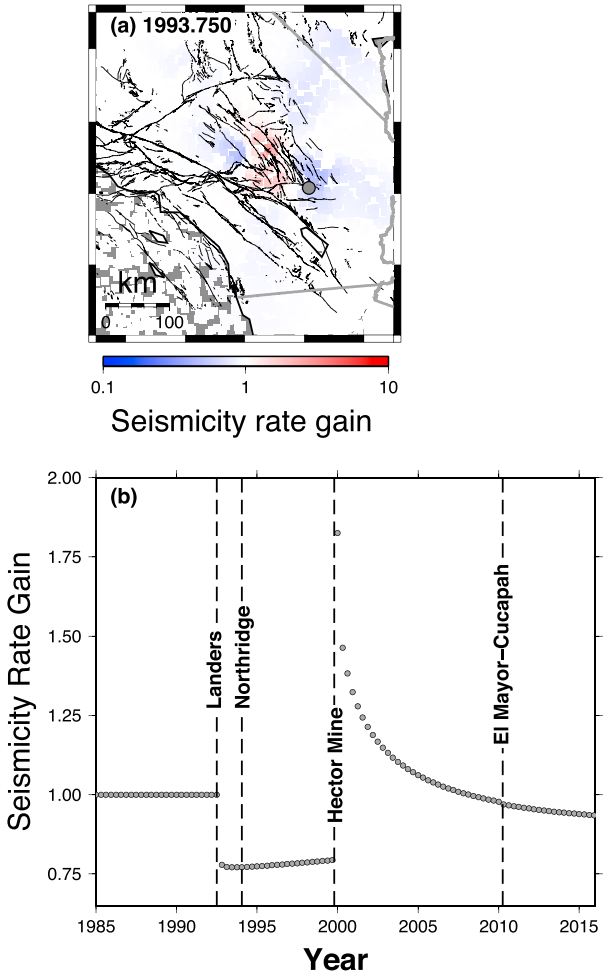

Figure 8. (a) Snapshot of seismicity rate gain R/r at the randomly distributed hypocenters, evaluated 1.25 years after the Landers quake, for one realization of random selection of focal mechanism solution for each catalog hypocenter. Gray areas are devoid of coverage by the set of random hypocenters. (b) Time series of model predicted R/r at the location of one of the random hypocenters (gray circle) indicated in Figure 8a.

$$\mathrm{LL} = \sum_i \log\left[R(\mathbf{r}_i, t_i)\right] - \int\int R(\mathbf{r}, t)\, \mathrm{d}^3\mathbf{r}\, \mathrm{d}t, \tag{10}$$

where $(\mathbf{r}_i, t_i)$ is the hypocenter and occurrence time of event #i in the observed seismicity catalog and the integration in the second term is over the volume of the study region and the time span since the first perturbing event, i.e., the time of the 1992 Landers quake through 2014. The first term of LL is calculated using estimates of R at the catalog hypocenters, whereas the second term of LL is calculated using estimates of R from 3000 randomly distributed points in the study volume.

From equations (4)–(9), the seismicity rate R at a given location depends upon the assigned receiver fault geometry. At the locations of observed hypocenters this is specified directly. The Hauksson catalog includes focal mechanism determinations derived from waveform cross correlation [*Yang et al.*, 2012; *Hauksson et al.*, 2012], and thus, it provides information on the geometry of potentially triggered events. The focal mechanism information provides two slip planes and directions to define each rupture, which provides two alternate estimates of Coulomb stress change for a given incident stress field. At the locations of the random hypocenters, we impose the simple rule that the assigned $\hat{\boldsymbol{n}}$ and $\hat{\boldsymbol{s}}$ equal that specified at the nearest catalog hypocenter.

The seismicity rate also depends upon the stressing rate $\dot{\tau}_i$. We determine the stressing rate field using the horizontal strain rate field derived from the GPS velocity field [*Pollitz et al.*, 2010]. It is assumed in this procedure

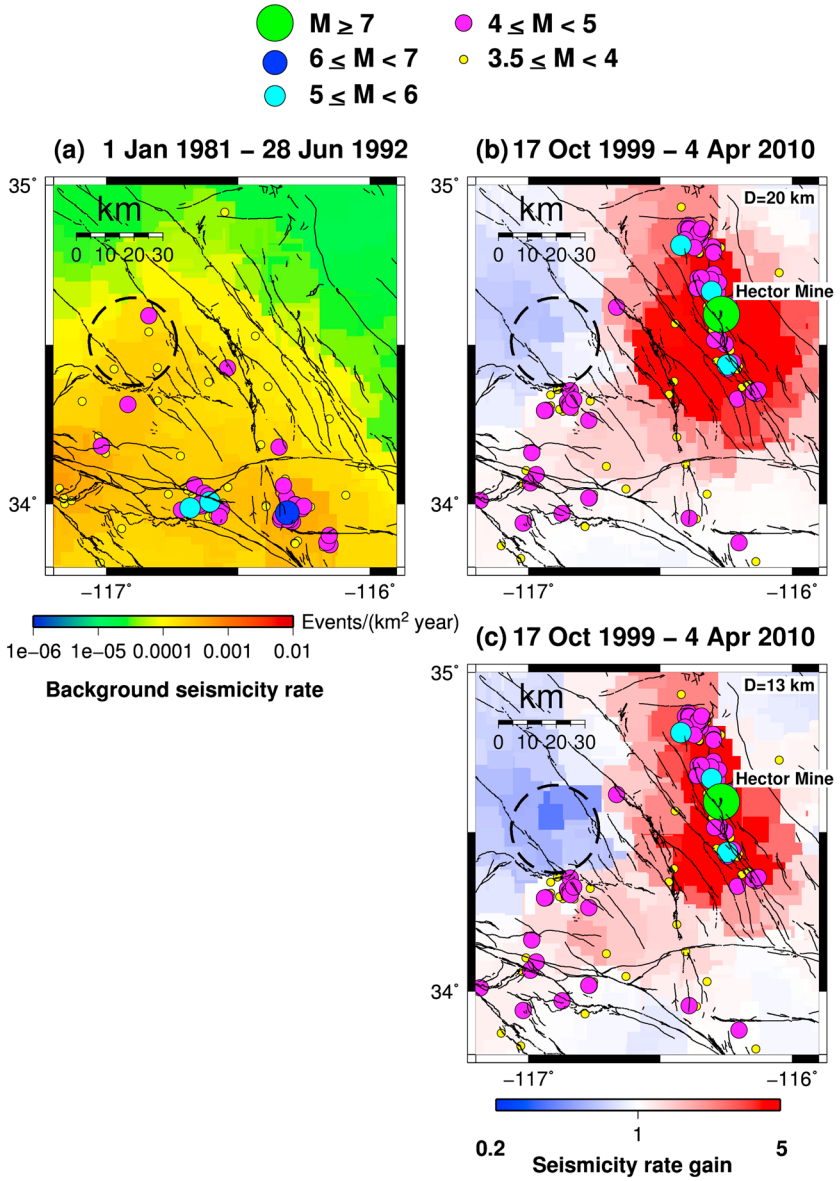

Figure 9. (a) Background seismicity rate during the 11.5 years prior to the Landers quake (extracted from Figure 3b). Superimposed are the epicenters of $M \geq 3.5$ seismicity in Southern California from 1981 to just before the 1992 Landers quake (extracted from Figure 1a). (b) Predicted average seismicity rate gain R/r over a 10.4 year time period between the Hector Mine and El Mayor-Cucapah earthquakes using $D(\mathbf{r}) = 20$ km in equation (11). (c) Same as Figure 9b with $D(\mathbf{r}) = 13$ km. Superimposed are the epicenters of $M \geq 3.5$ seismicity during that time period. The area indicated by the dashed circle has low rates in Figures 9b and fig9c but a high rate in 9a.

that the surface strain rate field is representative of the strain field at depth, which may be accurate within the uppermost crust where a frictional rheology dominates, but it is less accurate near the brittle-ductile transition where the strain rate field is expected to undergo large perturbations [e.g., *Takeuchi and Fialko*, 2012]. This strain rate field is converted into a stressing rate field, and at a dense sample of points covering the study area the second invariant of the stressing rate tensor is evaluated [*Jaeger and Cook*, 1984, equation (2.11)]. The resulting map of stressing rates is smoothed at a length scale of 20 km to provide $\dot{\tau}_t$ at catalog hypocenters and random hypocenters. Stressing rates $\dot{\tau}_r$ at the random hypocenters derived from this procedure are shown in Figure 6.

When employing equation (7) to evaluate seismicity rate, a common difficulty is that events may occur in the stress shadow of previous events, where ΔS may be very low, and hence, from equations (5) and (6),

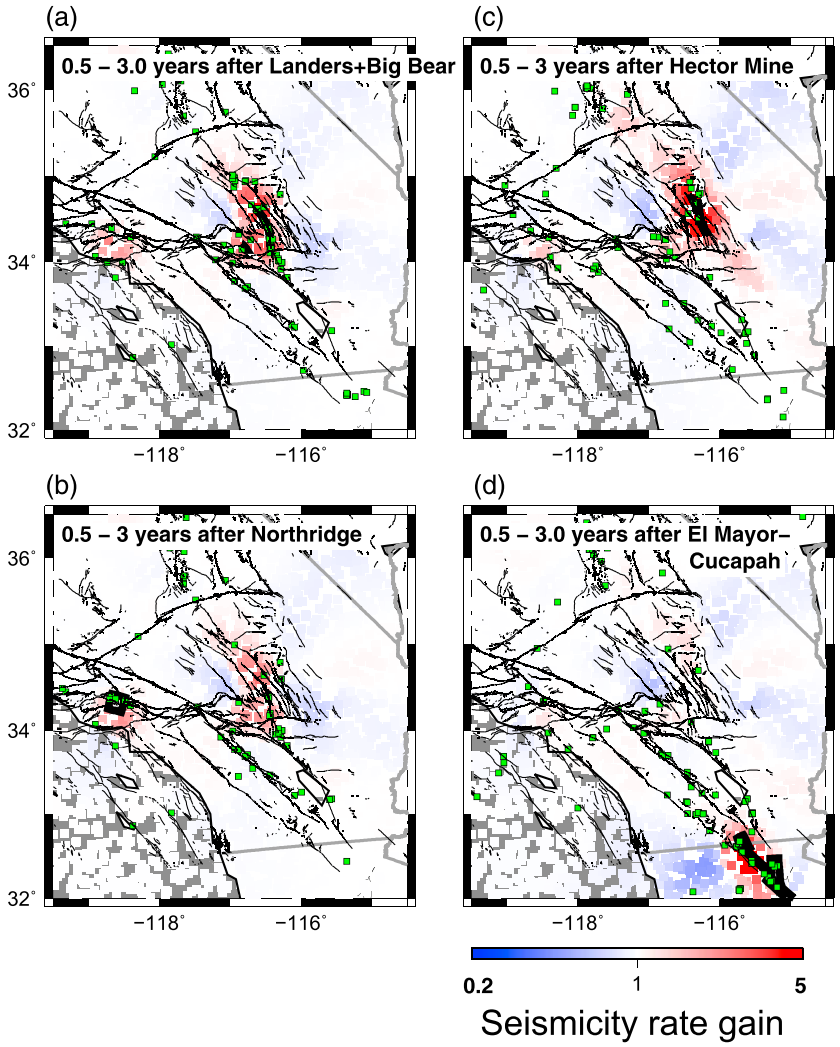

Figure 10. Predicted average seismicity rate gain R/r over 2.5 year long time intervals following each of four $M \geq 6.7$ source quakes, for one realization of a random selection of focal mechanism solutions, evaluated at the random hypocenter locations: (a) after the Landers quake, (b) after the Northridge quake, (c) after the Hector Mine quake, and (d) after the El Mayor-Cucapah quake. Gray areas are devoid of coverage by the set of random hypocenters. Outlines of source faults are shown with thick black lines in each subplot. Observed seismicity with *Knopoff* [2000] declustering is superimposed with green squares.

γ may be extremely large [e.g., *Segou and Parsons*, 2014; *Cattania et al.*, 2014]. Very large model γ, and hence low R, evaluated in a shadow zone will generally persist well beyond the early postseismic period. Previous studies have shown that stress shadows are drastically reduced in rate and state when considering small-scale (unresolved) heterogeneity in the stress field [*Marsan*, 2006; *Helmstetter and Shaw*, 2006; *Cattania et al.*, 2014]. Therefore, the presence of predicted strong stress shadows, and consequently unrealistically low predicted seismicity rates, reflects to a large extent uncertainty in the source models plus the ignorance of other physics that may promote triggering in a shadow of a main shock, e.g., secondary stress changes on nearby faults [*Segou and Parsons*, 2014]. To circumvent this problem, we introduce smoothing of the reciprocal of the state variable, γ^{-1}. We employ Gaussian smoothing using the modeled γ at the catalog hypocenters $\mathbf{r}_i$ to estimate the smoothed reciprocal state variable $\bar{\gamma}^{-1}$ via

$$\bar{\gamma}^{-1}(\mathbf{r},t) = \frac{\sum_i \exp\left(-\frac{1}{2}\left[|\mathbf{r}-\mathbf{r}_i|/D(\mathbf{r})\right]^2\right)\gamma^{-1}(\mathbf{r}_i,t)}{\sum_i \exp\left(-\frac{1}{2}\left[|\mathbf{r}-\mathbf{r}_i|/D(\mathbf{r})\right]^2\right)}. \quad (11)$$

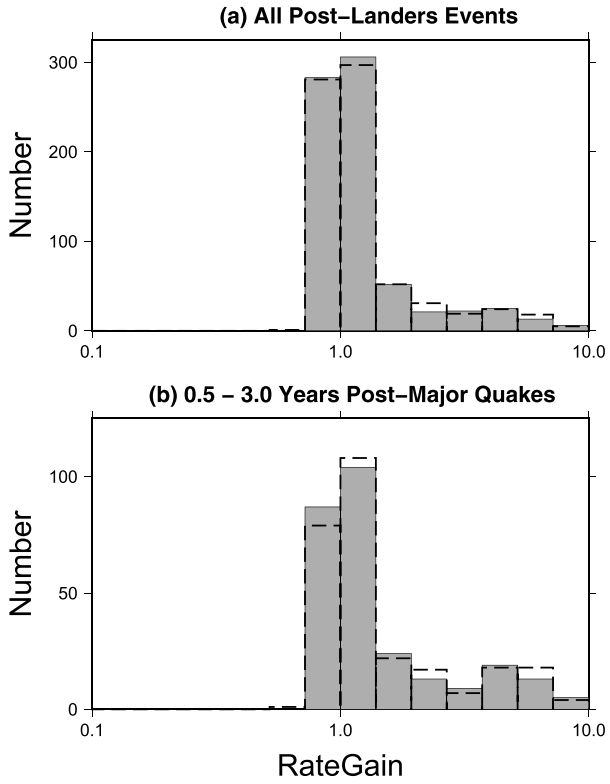

Figure 11. Histogram of predicted seismicity rate gain R/r at the times and locations of catalog events from just after the Landers quake to the end of 2014, for one realization of a random selection of focal mechanism solutions. (a) All events from 28 June 1992 (just after the Landers quake) to 31 December 2014. (b) All events over 2.5 year long time intervals following each of four $M \geq 6.7$ source quakes. *Knopoff* [2000] declustering has been applied to observed seismicity. Continuous lines with shading correspond to $\mu' = 0.2$; dashed lines correspond to $\mu' = 0.6$.

The same spatial averaging should be applied to the background stressing rate. Time-dependent seismicity rate is then a revision of equation (7):

$$R = \bar{\gamma}^{-1} \frac{r}{\dot{\bar{\tau}}_r}. \tag{12}$$

We find that, in practice, this ameliorates the problem of large negative LL values driven by locally large negative stress changes δS but at the cost of eliminating short wavelength variations in the state variable and hence in the time-dependent seismicity rate R. Accepting this simplification is an acknowledgment that the state variable and hence theoretical seismicity rate, especially close to the source rupture, are influenced by factors other than the static stress change. For example, dynamic wave propagation effects may reduce γ induced by reduction of the mean critical slip distance [*Parsons*, 2005], and this would counteract the tendency of a stress shadow to increase γ, thus making events more likely to occur in stress shadows than they would otherwise be.

4.3. Testing the Stress Evolution Model

The importance of stress evolution for driving regional seismicity may be visualized by examining the time-dependent seismicity rate gain R/r and comparing with regional seismicity. In doing so, we decluster the observed seismicity according to the *Knopoff* [2000] prescription. This is done to remove the earliest aftershocks, which are affected by numerous processes apart from static and viscoelastic stress transfer. In particular, up to 40% of aftershocks occurring close to a $M \geq 7$ main shock globally are thought to be attributable to dynamic stressing [*Parsons*, 2002]; *van der Elst and Brodsky* [2010] estimate that 15% to 60% of near-field aftershocks of $M3-5.5$ main shocks are attributable to dynamic stressing. Early aftershocks are also likely influenced by afterslip and secondary triggering [*Cattania et al.*, 2015]. The Coulomb rate-and-state model based on *Dieterich* [1994] presented in section 2 assumes that aftershock nucleation sites do not interact with each other; hence, secondary triggering is not included in our model. By removing the

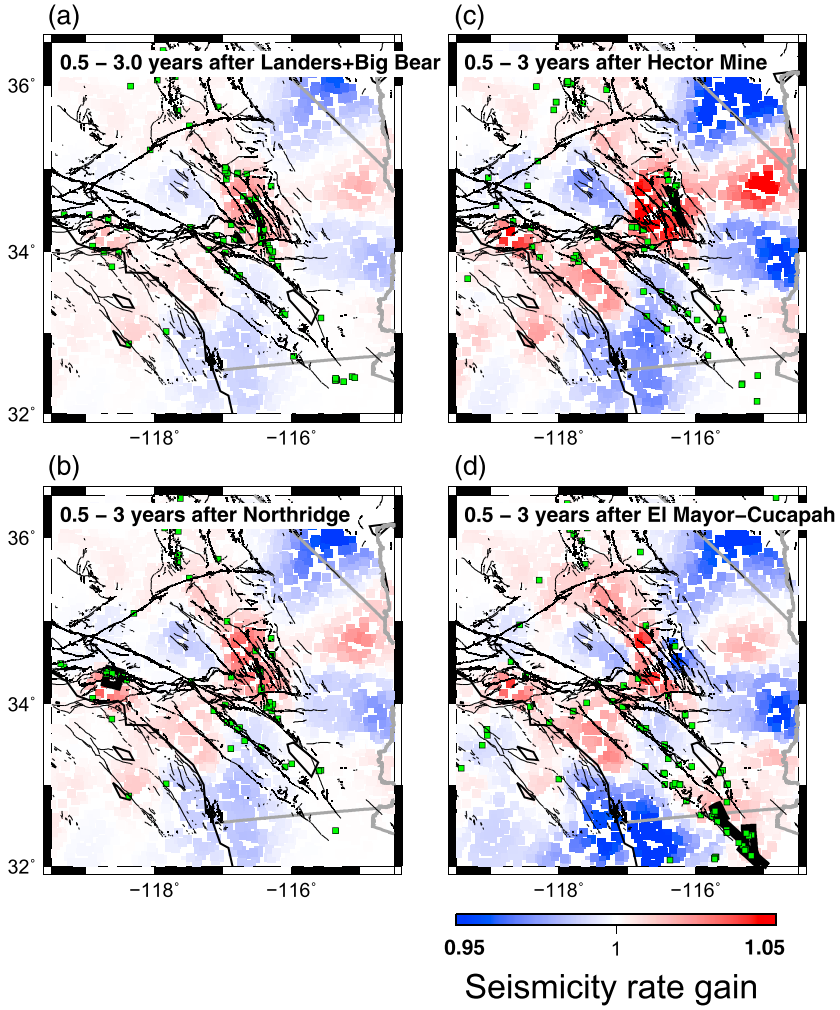

Figure 12. Predicted average seismicity rate gain $R_{\text{coseismic+postseismic}}/R_{\text{coseismic}}$ over 2.5 year long time intervals following each of four $M \geq 6.7$ source quakes, for one realization of a random selection of focal mechanism solutions, evaluated at the random hypocenter locations: (a) after the Landers quake, (b) after the Northridge quake, (c) after the Hector Mine quake, and (d) after the El Mayor-Cucapah quake. Outlines of source faults are shown with thick black lines in each subplot. Observed seismicity with *Knopoff* [2000] declustering is superimposed with green squares.

earliest aftershocks, we are focusing on that part of the seismicity that we believe is more strongly shaped by static and/or viscoelastic stress transfer. Cumulative seismicity with the original catalog may compared with the declustered catalog in Figure 7, which shows that most early aftershocks are removed with declustering.

In the following examples, we extract one realization of random selection of focal mechanism solutions from the two available solutions for each catalog hypocenter; this specifies the geometry of both actual catalog events and random events as described in the previous section. We specify an effective friction coefficient $\mu' = 0.2$ and an aftershock decay time $t_a = 5000$ days.

Figure 8a has a snapshot of R/r 1.25 years after the Landers quake, and Figure 8b shows time series of R/r at a random hypocenter located near the southern terminus of the Hector Mine rupture. Rate changes associated with large negative and positive stress steps are seen at the time of the Landers and Hector Mine earthquakes, respectively. The sharp decline in R/r after the positive stress step following the Hector Mine quake is to be contrasted with the gradual increase in R/r after the negative stress step following the Landers quake. This exemplifies that stress shadows persist much longer than positively stressed regions, a fact which is highlighted by the fact that R/r diminishes below unity after 2010 despite the earlier positive stress step in 1999. Although we do not quantify how predicted shadows correlate with observed seismicity rate reductions, we note that a seismicity rate reduction is observed ~70 km west of the Hector Mine rupture (compare seismicity

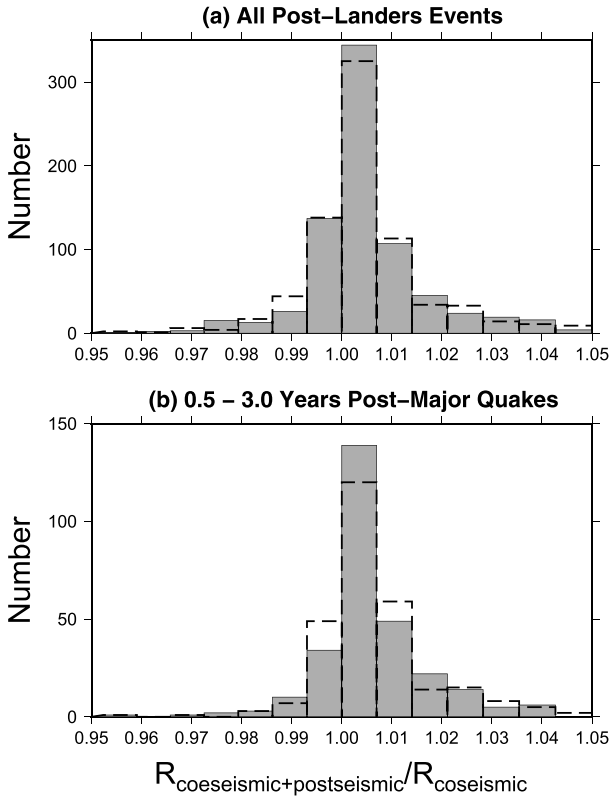

Figure 13. Histogram of predicted seismicity rate gain $R_{\text{coseismic+postseismic}}/R_{\text{coseismic}}$ at the times and locations of catalog events, for one realization of a random selection of focal mechanism solutions. (a) All events from 28 June 1992 (just after the Landers quake) to 31 December 2014. (b) All events over 2.5 year long time intervals following each of four $M \geq 6.7$ source quakes. *Knopoff* [2000] declustering has been applied to observed seismicity. Continuous lines with shading correspond to $\mu' = 0.2$; dashed lines correspond to $\mu' = 0.6$.

within the dashed circles in Figures 9a and 9b). This agrees qualitatively with predicted low-seismicity rate gain R/r for several years following the combined Landers and Hector Mine ruptures (Figures 9b and 9c).

To test the coherence of predicted R/r with observed seismicity, we consider a set of time intervals of length 2.5 years beginning 0.5 years after each $M \geq 6.7$ source quake. These time intervals sample the postseismic period of each source quake without the earliest postshocks, and we further decluster the observed seismicity according to the *Knopoff* [2000] prescription. Comparison between observed R/r and seismicity after each source (Figure 10) quake exhibits a visual correlation between positive predicted seismicity rate gain and observed seismicity.

This pattern is further quantified by examining a histogram of rate gain using the totality of post-Landers quake catalog events. The summary of predicted R/r at the times and locations of the post-Landers events, again edited with the *Knopoff* [2000] prescription, is shown in Figure 11a. It reveals a tendency for post-Landers seismicity to occur where modeled combined coseismic and postseismic stress changes tend to produce seismicity rate gain at the times and locations of catalog events. This tendency is maintained when the first 0.5 years following each $M \geq 6.7$ source quake is excluded (Figure 11b), showing that the pattern is not dictated by vigorous aftershock activity following the largest regional events.

The impact of postseismic stressing on predicted seismicity rates may be evaluated by considering the average "postseismic seismicity rate gain" $R_{\text{coseismic+postseismic}}/R_{\text{coseismic}}$, which is a ratio of the predicted seismicity rates using stress evolution models including coseismic and postseismic stresses and only coseismic stresses, respectively. The pattern of postseismic seismicity rate gain in the same 2.5 year long time intervals considered previously is shown in Figure 12. It reveals that up to $\pm$ ~5% rate gain is attributable to postseismic stresses. Moreover, most of the seismicity occurring more than 0.5 years after the major source quakes is located in one of the four quadrants of positive rate gain. This is verified by examination of histograms of postseismic rate

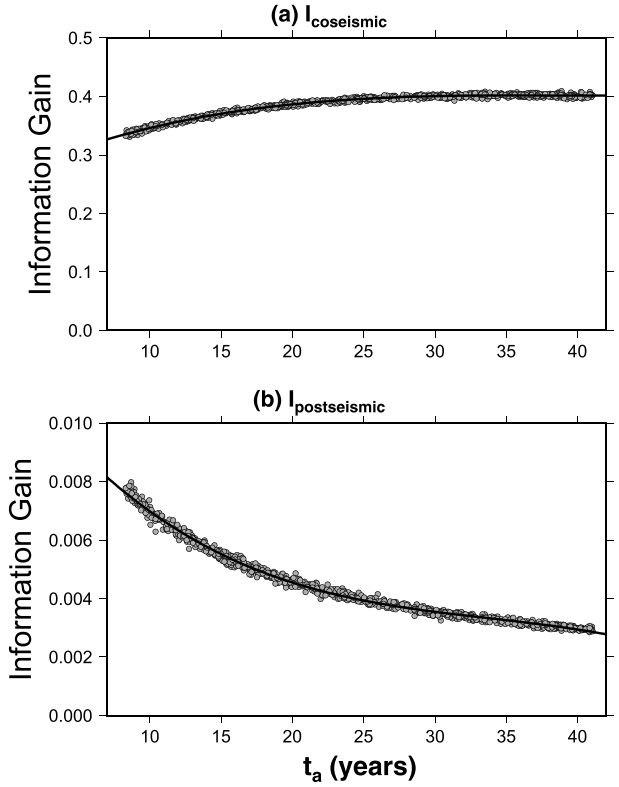

Figure 14. Information gain (equation (13)) as a function of t_a for 1000 realizations of random selections of focal mechanism solutions for 726 post-Landers events. (a and b) The information gains $I_{\text{coseismic}}$ and $I_{\text{postseismic}}$, respectively, are defined in section 5. In each case, the best fitting cubic curve through the plotted points is superimposed as a continuous line.

gain using either events spanning the entire post-Landers epoch (up to the end of 2014) (Figure 13a) or events within the 2.5 year long time intervals beginning 0.5 years after each $M \geq 6.7$ source quake (Figure 13b).

Seismicity rates along the San Jacinto Fault Zone have been highly variable for the past 25 years (Figure 1). Decreased earthquake activity along the central San Jacinto fault following the Landers earthquake (Figure 1b) is correlated with seismicity rate gains of ~0.95, i.e., less than 1 (Figures 8a and 10). Increased earthquake productivity along the southernmost San Jacinto fault and Elsinore fault for several months following the El Mayor-Cucapah earthquake [*Meng and Peng*, 2014] is correlated with seismicity rate gains of ~1.05 (Figure 10). However, earthquake activity along the remainder of the San Jacinto fault documented by *Meng and Peng* [2014] is not well correlated with coseismic or postseismic stressing predicted by the Coulomb rate-state model (Figures 10 and 12). Its exceptional activity may be attributed to a combination of dynamic triggering and transient loading along the deeper section of the fault as proposed by *Wdowinski* [2009] and *Lindsey et al.* [2014] and recently documented by *Inbal* [2017].

Figures 11 and 13 include the seismicity rate gain histograms for the case where $\mu' = 0.6$ (dashed lines). There is little difference between these and the corresponding histograms obtained using $\mu' = 0.2$, and in remaining simulations we shall assume $\mu' = 0.2$.

5. Discussion

The systematic pattern of post-Landers earthquake occurrence being associated with both positive coseismic plus postseismic stress $R_{\text{coseismic+postseismic}}/r$ (Figures 10 and 11) and positive postseismic stress $R_{\text{coseismic+postseismic}}/R_{\text{coseismic}}$ (Figures 12 and 13) may be further examined using the information gain defined by

$$I = \frac{\text{LL} - \text{LL}_0}{N}, \tag{13}$$

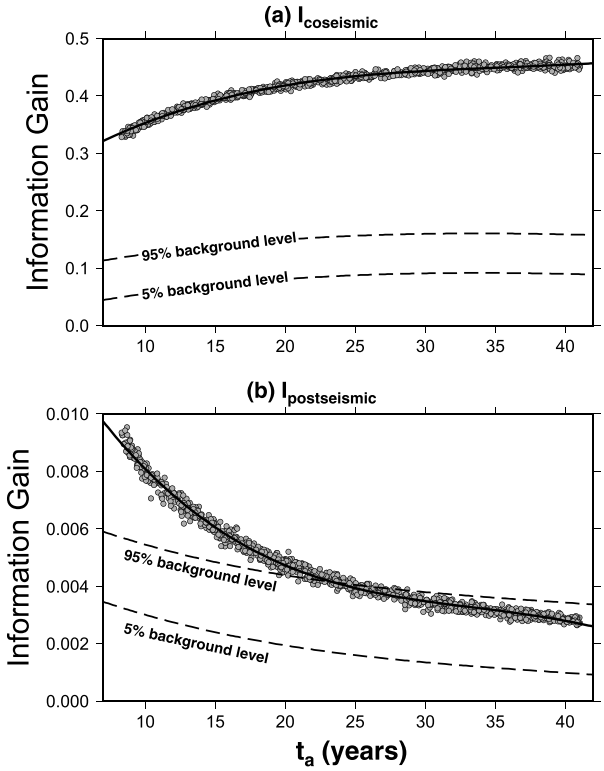

Figure 15. Information gain (equation (13)) as a function of t_a for 1000 realizations of random selections of focal mechanism solutions for 280 post-Landers events, which have been restricted to a set of time intervals of length 2.5 years beginning 0.5 years after each $M \geq 6.7$ source quake. (a and b) The information gains $I_{coseismic}$ and $I_{postseismic}$, respectively, are defined in section 5. In each case, the best fitting cubic curve through the plotted points is superimposed as a continuous line. Dashed lines are the 5% and 95% curves of obtained $I_{coseismic}$ and $I_{postseismic}$ taken from Figure 16.

where LL_0 is the log likelihood evaluated for a reference model and N is the number of earthquakes occurring in a specified space and time window.

Given the ambiguity of focal plane, we randomize the selection of focal plane for each event between the catalog focal plane and the corresponding auxiliary plane. We simultaneously sample t_a to lie between 3000 and 15,000 days (8.2 and 41.1 years). We assume that the same aftershock time scale is applicable to the sequences following all main shocks regardless of their magnitude. This is a simplification of the physics because larger main shocks may have larger t_a, e.g., inferred $t_a = 25-50$ years for the Landers main shock versus $t_a = 7$ years for the Big Bear main shock [*Toda et al.*, 2005, Table 2]. After declustering, a total of $N = 726$ post-Landers events is admitted. With a Monte Carlo simulation of 1000 realizations of random sets of focal planes and t_a, the corresponding distribution of I as a function of t_a is shown in Figure 14. We first assess the importance of coseismic stressing, defining $I = I_{coseismic}$ using a log likelihood LL that includes coseismic stressing and a reference log likelihood LL_0 with no stress perturbation, i.e., $\gamma = \frac{1}{\tau_r}$ and $R = r$ (Figure 14a). We next assess the importance of postseismic stressing, defining $I = I_{postseismic}$ using a log likelihood LL that includes coseismic and postseismic stressing and a reference log likelihood LL_0 based on coseismic stressing (Figure 14b); in both cases, I is significantly greater than zero. The scatter in the patterns arises from the fact that the friction coefficient μ' is nonzero; in either case, all realizations would collapse onto a straight line if μ' are zero because then the ambiguity is focal plane is immaterial.

Generally, higher information gains are attained are if seismicity is restricted to time intervals of length 2.5 years beginning 0.5 years after each $M \geq 6.7$ source quake. In this case, after declustering, a total of $N = 280$ post-Landers events is admitted. For the ensemble of these four 2.5 year long periods following each source quake, $I_{coseismic}$ (Figure 15a) has increased by 5–10% relative to the $I_{coseismic}$ attained using all declustered post-Landers seismicity (Figure 14a). For $t_a < 20$ years, $I_{postseismic}$ (Figure 15b) is also about 5–10 % greater than the $I = I_{postseismic}$ attained using all declustered post-Landers seismicity (Figure 14b). At $t_a > 20$ years, the

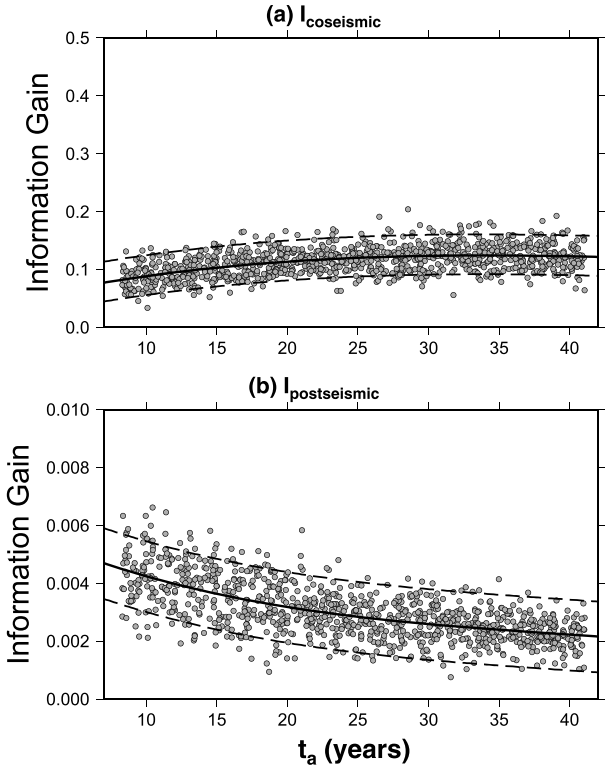

Figure 16. Information gain (equation (13)) as a function of t_a for 1000 realizations of random selections of focal mechanism solutions for 280 post-Landers events, which have been restricted to a set of time intervals of length 2.5 years beginning 0.5 years after each $M \geq 6.7$ source quake. Compared with Figure 15, for each post-Landers event, the origin time is preserved but the location is exchanged for a randomly chosen pre-Landers event. (a and b) The information gains $I_{coseismic}$ and $I_{postseismic}$, respectively, are defined in section 5. In each case, the best fitting cubic curve through the plotted points is superimposed as a continuous line, and shifted cubic curves encompassing 5% or 95% of the plotted points are superimposed as dashed lines.

postseismic information gains are similar in the two cases. These patterns suggest that seismicity occurring in the 6 months following the $M \geq 6.7$ source quakes is controlled by other factors besides coseismic and postseismic stressing. This could include dynamic stressing [e.g., *Freed*, 2005] or secondary aftershock triggering, as was proposed for the *M*7.3 1992 Landers-to-*M*7.1 1999 Hector Mine, California, earthquake sequence [*Felzer et al.*, 2002].

While the foregoing tests demonstrate spatial coherence of post-1992 Landers seismicity with predicted areas of coseismic and postseismic stressing, they leave open the possibility that seismicity always tends to concentrate in these zones, i.e., pre-Landers seismicity might spatially correlate with areas of predicted post-Landers elevated seismicity rate. To address this, we repeat the exercise of evaluating information gains for the ensemble of 2.5 year periods beginning 0.5 years after each $M \geq 6.7$ source quake. For each of the 280 admitted post-Landers events, we preserve the origin time but exchange its location with a randomly chosen pre-Landers event. The resulting patterns of $I_{coseismic}$ and $I_{postseismic}$ as a function of t_a (Figure 16) are lower than their counterparts in Figure 15, especially for the coseismic information gain. Figure 16 includes dashed curves above which 5% or 95% of the simulated information gains fall. These curves are repeated for reference in Figure 15, where they represent the tails of distributions of coseismic and postseismic information gains using background seismicity hypocenters in place of actual hypocenters. They confirm that the coseismic information gain in Figure 15 is much higher than is attainable from the spatial distribution of background seismicity, and the same is true for the postseismic information gain for $t_a \lesssim 20$ years. Estimates of t_a for the plate boundary zone of Southern California based on observed aftershock sequences tend to be less than 20 years [*Toda et al.*, 2005; *Stein and Liu*, 2009]. This strongly suggests that the spatial pattern of seismicity shifted systematically after the Landers quake to be preferentially concentrated in zones of predicted elevated crustal stress affected by combined coseismic and postseismic stress changes following the major source quakes. This is a confirmation of the same conclusion reached by *Toda et al.* [2005] as measured by seismicity-rate

correlation coefficient or by *Strader and Jackson* [2015] based on activation probabilities of observed seismicity as a function of CFF.

6. Conclusions

Seismic activity in Southern California over the past three decades has been concentrated on sections of the SAF, San Jacinto fault, Elsinore fault, and Eastern California Shear Zone primarily through right-lateral strike-slip faulting and around the blind thrust faults that accommodate convergent plate motion near the Big Bend. Crustal stress is time dependent and affected by coseismic stress steps and viscoelastic relaxation of the lower crust and mantle following major earthquakes. We have employed four $M \geq 6.7$ quakes since 1992 (including the *M*6.5 Bear Bear event as part of the Landers sequence) for this purpose and use a 2-D viscoelastic structure to estimate time-dependent stressing. Seismicity at magnitude $M \geq 3.5$ since the *M*7.3 1992 Landers quake occurs preferentially within areas that have a model-predicted positive Coulomb stress change at the time and location of the quake. This result is based on a declustered seismicity catalog and is robust even when the catalog is further edited to remove quakes occurring within the first 6 months following a major ($M \geq 6.7$) event. Postseismic stressing is also found to have altered the long-term spatial pattern of seismicity compared with background seismicity, especially for lower aftershock decay times $t_a \lesssim 20$ years. Hence, the post-Landers shift in seismicity pattern is accentuated by postseismic stressing, suggesting that the viscoelastic relaxation process has a tangible effect on determining the location and timing of Southern California seismicity.

Acknowledgments
We are grateful to Tom Parsons and Margarita Segou for internal reviews. This paper benefitted from the constructive criticisms of Shinji Toda, an anonymous reviewer, and Editor Yehuda Ben-Zion. The seismicity catalog used in this paper originates from Egill Hauksson and was downloaded from http://scedc.caltech.edu/research-tools/alt-2011-yang-hauksson-shearer.html.

References

Cattania, C. (2015), Improvement of aftershock models based on Coulomb stress changes and rate-and-state-dependent friction, PhD thesis, Univ. of Potsdam, Potsdam, Germany.
Cattania, C., S. Hainzl, L. Wang, F. Roth, and B. Enescu (2014), Propagation of Coulomb stress uncertainties in physics-based aftershock models, *J. Geophys. Res. Solid Earth*, *119*, 7846–7864, doi:10.1002/2014JB011183.
Cattania, C., S. Hainzl, L. Wang, B. Enescu, and F. Roth (2015), Aftershock triggering by postseismic stresses: A study based on Coulomb rate-and-state models, *J. Geophys. Res. Solid Earth*, *120*, 2388–2407, doi:10.1002/2014JB011500.
DeVries, P. M. R., P. G. Krastev, and B. J. Meade (2016), Geodetically constrained models of viscoelastic stress transfer and earthquake triggering along the North Anatolian fault, *Geochem. Geophys. Geosyst.*, *17*, 2700–2716, doi:10.1002/2016GC006313.
Dieterich, J. H. (1994), A constitutive law for rate of earthquake production and its application to earthquake clustering, *J. Geophys. Res.*, *99*, 2601–2618.
Felzer, K. R., T. W. Becker, R. E. Abercrombie, G. Ekström, and J. R. Rice (2002), Triggering of the 1999 M_w 7.1 Hector Mine earthquake by aftershocks of the 1992 M_w 7.3 Landers earthquake, *J. Geophys. Res.*, *107*(B9), 2190, doi:10.1029/2001JB000911.
Freed, A. M. (2005), Earthquake triggering by static, dynamic, and postseismic stress transfer, *Ann. Rev. Earth Planet. Sci.*, *33*, 335–367, doi:10.1146/annurev.earth.33.092203.122505.
Freed, A. M., and J. Lin (2001), Delayed triggering of the 1999 Hector Mine earthquake by viscoelastic stress transfer, *Nature*, *411*, 180–183.
Gardner, J. K., and L. Knopoff (1974), Is the sequence of earthquakes in Southern California, with aftershocks removed, Poissonian?, *Bull. Seismol. Soc. Am.*, *64*, 1363–1367.
Hainzl, S., S. Steacy, and D. Marsan (2010), Seismicity models based on Coulomb stress calculations, *Community Online Resource for Statistical Seismicity Analysis*, doi:10.5078/corssa-32035809.
Harris, R. A. (1998), Introduction to special section: Stress triggers, stress shadows, and implications for seismic hazard, *J. Geophys. Res.*, *103*, 24,347–24,358.
Hauksson, E., L. M. Jones, and K. Hutton (1995), The 1994 Northridge earthquake sequence in California: Seismological and tectonic aspects, *J. Geophys. Res.*, *100*, 12,335–12,355.
Hauksson, E., W. Yang, and P. M. Shearer (2012), Waveform relocated earthquake catalog for Southern California (1981–2011), *Bull. Seismol. Soc. Am.*, *102*, 2239–2244, doi:10.1785/0120120010.
Helmstetter, A., and B. E. Shaw (2006), Relation between stress heterogeneity and aftershock rate in the rate-and-state model, *J. Geophys. Res.*, *111*, B07304, doi:10.1029/2005JB004077.
Helmstetter, A., Y. Y. Kagan, and D. D. Jackson (2007), High-resolution time-independent grid-based forecast for M≥5 earthquakes in California, *Seismol. Res. Lett.*, *78*, 78–86, doi:10.1785/gssrl.78.1.78.
Inbal, A. (2017), Seismogeodetic imaging of active crustal faulting, PhD thesis, Calif. Inst. of Technol., Pasadena, Calif.
Jaeger, J. C., and N. G. W. Cook (1984), *Fundamentals of Rock Mechanics*, Chapman and Hall Ltd., New York.
Jones, L. E., S. E. Hough, and D. V. Helmberger (1993), Rupture process of the June 28, 1992 Big Bear earthquake, *Geophys. Res. Lett.*, *20*, 1907–1910.
Jónsson, S., H. Zebker, P. Segall, and F. Amelung (2002), Fault slip distribution of the 1999 M_w 7.1 Hector Mine, California, earthquake estimated from satellite radar and GPS measurements, *Bull. Seismol. Soc. Am.*, *92*, 1377–1389.
King, G. C., R. S. Stein, and J. Lin (1994), Static stress changes and the triggering of earthquakes, *Bull. Seismmol. Soc. Am.*, *84*, 935–954.
Knopoff, L. (2000), The magnitude distribution of declustered earthquakes in Southern California, *Proc. Nat. Acad. Sci.*, *97*, 11,880–11,884.
Lindsey, E. O., V. J. Sahakian, Y. Fialko, Y. Bock, S. Barbot, and T. K. Rockwell (2014), Interseismic Strain Localization in the San Jacinto Fault Zone, *Pure Appl. Geophys.*, *97*, 2937–2954, doi:10.1007/s00024-013-0753-z.
Linker, M. F., and J. H. Dieterich (1992), Effects of variable normal stress on rock friction: Observations and constitutive equations, *J. Geophys. Res.*, *97*, 4923–4940.
Marsan, D. (2006), Can coseismic stress variability suppress seismicity shadows? Insights from a rate-and-state friction model, *J. Geophys. Res.*, *111*, B06305, doi:10.1029/2005JB004060.

Meng, X., and Z. Peng (2014), Seismicity rate changes in the Salton Sea Geothermal field and the San Jacinto Fault Zone after the 2010 M_W 7.2 El Mayor-Cucapah earthquake, *Geophys. J. Int.*, *197*, 1750–1762, doi:10.1093/gji/ggu085.
Ogata, Y. (1983), Estimation of the parameters in the modified Omori formula for aftershock frequencies by the maximum likelihood procedure, *J. Phys. Earth*, *31*, 115–124.
Parsons, T. (2002), Global Omori law decay of triggered earthquakes: Large aftershocks outside the classical aftershock zone, *J. Geophys. Res.*, *107*(B9), 2199, doi:10.1029/2001JB000646.
Parsons, T. (2005), A hypothesis for delayed dynamic earthquake triggering, *Geophys. Res. Lett.*, *32*, L04302, doi:10.1029/2004GL021811.
Pollitz, F. F. (2014), Post-earthquake relaxation using a spectral element method: 2.5-D case, *Geophys. J. Int.*, *198*, 308–326, doi:10.1093/gji/ggu114.
Pollitz, F. F. (2015), Post-earthquake relaxation evidence for laterally variable viscoelastic structure and water content in the Southern California mantle, *J. Geophys. Res. Solid Earth*, *120*, 2672–2696, doi:10.1002/2014JB011603.
Pollitz, F. F., and I. S. Sacks (2002), Stress triggering of the 1999 Hector Mine earthquake by transient deformation following the 1992 Landers earthquake, *Bull. Seismol. Soc. Am.*, *92*, 1487–1496.
Pollitz, F. F., P. McCrory, D. Wilson, J. Svarc, C. Puskas, and R. B. Smith (2010), Viscoelastic-cycle model of interseismic deformation in the northwestern United States, *Geophys. J. Int.*, *181*, 665–696.
Segou, M., and T. Parsons (2014), The stress shadow problem in physics-based aftershock forecasting: Does incorporation of secondary stress changes help?, *Geophys. Res. Lett.*, *41*, 3810–3817, doi:10.1002/2013GL058744.
Steacy, S., J. Gomberg, and M. Cocco (2005), Introduction to special section: Stress transfer, earthquake triggering, and time-dependent seismic hazard, *J. Geophys. Res.*, *110*, B05S01, doi:10.1029/2005JB003692.
Stein, R. S (1999), The role of stress transfer in earthquake triggering, *Nature*, *402*, 605–609.
Stein, S., and M. Liu (2009), Long aftershock sequences within continents and implications for earthquake hazard assessment, *Nature*, *462*, 87–89, doi:10.1038/nature08502.
Strader, A., and D. D. Jackson (2015), Static Coulomb stress-based Southern California earthquake forecasts: A pseudoprospective test, *J. Geophys. Res. Solid Earth*, *120*, 1667–1676, doi:10.1002/2014JB011297.
Takeuchi, C. S., and Y. Fialko (2012), Dynamic models of interseismic deformation and stress transfer from plate motion to continental transform faults, *J. Geophys. Res.*, *117*, B05403, doi:10.1029/2011JB009056.
Toda, S., R. S. Stein, K. Richards-Dinger, and S. B. Bozkurt (2005), Forecasting the evolution of seismicity in Southern California: Animations built on earthquake stress transfer, *J. Geophys. Res.*, *110*, B05S16, doi:10.1029/2004JB003415.
van der Elst, N. J., and E. E. Brodsky (2010), Connecting near-field and far-field earthquake triggering to dynamic strain, *J. Geophys. Res.*, *115*, B07311, doi:10.1029/2009JB006681.
Wald, D., and T. Heaton (1994), Spatial and temporal distribution of slip for the 1992 Landers, California, earthquake, *Bull. Seismol. Soc. Am.*, *84*, 668–691.
Wdowinski, S. (2009), Deep creep as a cause for the excess seismicity along the San Jacinto fault, *Nat. Geosci.*, *2*, 882–885.
Wei, S., et al. (2011), Superficial simplicity of the 2010 El Mayor-Cucapah earthquake of Baja California in Mexico, *Nat. Geosc.*, *4*, 615–618, doi:10.1038/ngeo1213.
Yang, W., E. Hausksoon, and P. Shearer (2012), Computing a large refined catalog of focal mechanisms for Southern California (1981–2010): Temporal stability of the style of faulting, *Bull. Seismol. Soc. Am.*, *102*, 1179–1194.
Zeng, Y. (2001), Viscoelastic stress-triggering of the 1999 Hector Mine earthquake by the 1992 Landers earthquake, *Geophys. Res. Lett.*, *28*, 3007–3010.
Zhuang, J., D. Harte, M. J. Werner, S. Hainzl, and S. Zhou (2012), Basic models of seismicity: Temporal models. Community Online Resource for Statistical Seismicity Analysis, doi:10.5078/corssa-79905851. [Available at http://www.corssa.org.]